Julia Schuler*
Jakob Herath
Norbert Kockmann

X-Ray-Based Tomographic Imaging for the Investigation of Laminar Mixing in Capillaries

Micro-computed tomography is a promising non-invasive imaging technology that offers high spatial resolution without requiring optical access. This opens the opportunity to analyze concentration fields in mixing equipment in 3D. To demonstrate the potential of the methodology, laminar mixing in helically coiled capillaries is investigated by tracking the radial distribution of potassium iodide along the main flow direction. Dean flow can be observed in the helically coiled capillaries, which intensifies with Reynolds number and decreasing effect of gravity.

Keywords: Dean flow, Helically coiled capillary, Micro-computed tomography, Three-dimensional concentration fields

Received: October 18, 2021; *accepted:* May 06, 2022

DOI: 10.1002/ceat.202100530

Supporting Information available online

1 Introduction

In chemical and pharmaceutical engineering, performing processes on a small scale is a desirable approach for smaller production quantities or highly specialized products [1]. Owing to the small equipment dimensions, the Reynolds number is typically low, meaning the flow is laminar and diffusion is the predominant mechanism for radial mixing [2]. Mixing can be enhanced by coiling the capillary [3]. In coiled capillaries, the existence of curvature leads to the formation of a secondary flow pattern caused by the centrifugal force. The so-called Dean vortices (Fig. 1) are superimposed with the flow in the main flow direction leading to a screw-shaped flow [4]. An extensive overview of the broad application possibilities is given in [3].

The main parameters affecting the secondary flow in a helically coiled capillary (HCC) are the Reynolds number Re[1)] = ud_i/ν, curvature, and torsion [5–7] that are represented in the dimensionless Dean number Dn (Eq. (1)) and modified torsion parameter T^* (Eq. (2)) [8]. In the equations, d_i and d_c are the inner capillary diameter and the coil diameter, and p is the pitch of the coil, see Fig. 1. For low Dn (low curvature), no or only weak Dean vortices are formed [9] that intensify with increasing Dn and lead to improved radial mixing [10–12]. Contrary, increasing torsion (decreasing T^*) results in poorer mixing [13].

$$Dn = Re\sqrt{\frac{d_i}{d_c}} \tag{1}$$

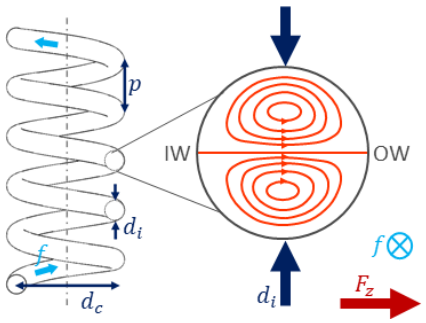

Figure 1. Helically coiled tube with qualitative depiction of Dean vortices and main geometric parameters. F_z indicates centrifugal force and f denotes the main flow direction.

$$T^* = \frac{Re\pi d_c}{p} \tag{2}$$

Flow fields in curved tubes were already visualized via holographic particle tracking [9], 2D and 3D particle image velocimetry (PIV) [14–18], and magnetic resonance imaging (MRI) [19, 20]. Recently, Kováts et al. applied laser-induced fluorescence to visualize concentration fields of a fluorescent dye at different angles of revolution [21]. So far, studies on X-ray-based computed tomography for the investigation of processes on the milli- to micro-scale are still rare [22] and only very few studies concern the direct investigation of mass transfer [23–25].

Julia Schuler, Jakob Herath, Prof. Dr. Norbert Kockmann
julia.schuler@tu-dortmund.de
Laboratory of Equipment Design, Department of Biochemical and Chemical Engineering, TU Dortmund University, 44227 Dortmund, Germany.

1) List of symbols at the end of the paper.

The current distribution is a step towards the X-ray-based tomographic investigation of mixing in capillary equipment. In X-ray imaging, X-rays with an initial intensity I_0 are attenuated by the sample. For idealized conditions (monochromatic X-ray beam), the attenuation process can be described by the Beer-Lambert law (Eq. (3)) [26]. Here, s constitutes the thickness of the sample and μ is the linear attenuation coefficient that strongly depends on the atomic number Z and the density ρ [26].

$$I = I_0 e^{-\mu s} \tag{3}$$

The remaining intensity I is measured at the detector, which gives a 2D projection image. For tomographic (3D) imaging, projection images must be acquired at several angles of rotation ω. This is achieved by either rotating sample and detector around the sample or by rotating the sample itself while keeping X-ray source and detector constant. The resulting set of 2D projection images is reconstructed to a virtual volume using a reconstruction algorithm. The virtual volume consists of a stack of cross-sectional slices built from voxels, the 3D equivalent to pixels.

2 Methods and Materials

2.1 Experimental Setup

For the X-ray-based visualization of laminar mixing, two fluids, one with and one without an X-ray contrast agent, are contacted and the distribution of the contrast agent along the main flow direction is tracked. The test helices consist of fluorinated ethylene propylene (FEP) tubes (d_i = 1.59 mm, d_o = 3.2 mm, Bohlender GmbH, Germany) which are coiled around a support structure (Fig. 2b) with d_c = 28.8 mm. The support structure is 3D printed from polylactide (PLA) using an ULTIMAKER S5 (Ultimaker, The Netherlands). Two setups are fabricated, one with pitch p_1 = 4.8 mm and another with p_2 = 9 mm. The lengths of the coiled tubes in the measurement sections are 30.2 cm for p_1 (φ_{max} = 1200°) and 18.2 cm for p_2 (φ_{max} = 720°). The first contact of the liquid containing contrast agent and pure liquid is realized in a commercially available T-junction (IDEX Health & Science, IDEX Corporation, Northbrook, IL), which is located below the actual measurement sections and hold in place by the support structure.

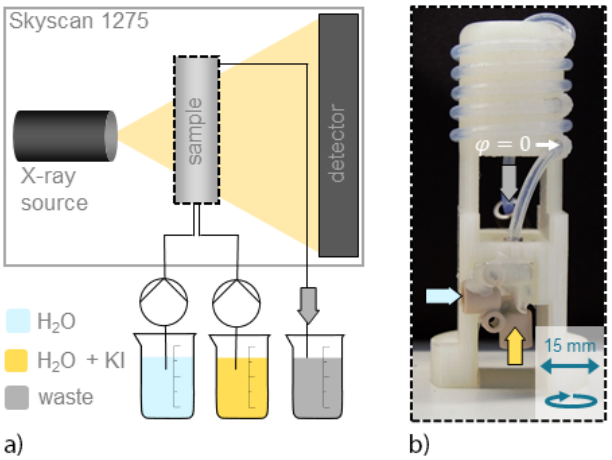

Figure 2. (a) Schematic overview of the experimental setup. (b) Setup for investigation of radial mixing.

The liquid containing the contrast agent is added through the bottom inlet and pure liquid through the side inlet of the T-junction. In this work, water is chosen as the liquid and potassium iodide (KI) is selected as the contrast agent as they show good X-ray contrast and the solubility of KI in water is high (144.5 g of KI per 100 g of water at T = 20 °C [27]), which allows for the preparation of solutions with high KI concentration. When dissolved in water, it forms K^+ and I^- ions, both having a significantly higher attenuation coefficient than water. However, as I^- (Z = 53) has a significantly higher mass attenuation coefficient than K^+ (Z = 19), only mass transfer of I^- is tracked using X-ray imaging [24].

Experiments are performed for different total volume flow rates $\dot{V}$, initial KI mass fractions $w_{KI,0}$, and pitches, see Tab. 1 [28]. The volume flow rate ratio of pure water and KI-enriched water is kept constant at a value of 1. Note that the properties of KI-enriched water differ from those of pure water. Densities for the calculation of dimensionless numbers are estimated from data given by Novotny and Sohnel [29] and dynamic viscosities are estimated from the data provided by Goldsack and Franchetto [30].

Table 1. Overview of flow experiments.

p [mm]	$w_{KI,0}$ [–]	$\dot{V}$ [mL min^{-1}]	Dimensionless numbers
–	–	–	Re = 23–185
4.8/9	0.05/0.015	1.5/3/5/7/12	Dn = 5–43
–	–	–	T^* = 436–3488

For tomographic imaging during the flow experiments, the helices are placed on the rotatable sample stage of the Bruker Skyscan 1275 (Bruker Skyscan 1275, RJL Micro & Analytic GmbH, Karlsdorf-Neuthart, Germany), a micro-computed tomography scanner with spatial resolutions up to 4 µm and maximum sample dimensions of diameter × height = 96 mm ×120 mm. Pulsation-free pumps (BlueShadow Pump 40P, KNAUER Wissenschaftliche Geräte GmbH, Berlin, Germany for pure water, LAMBDA VIT-FIT by LAMBDA Instruments GmbH, Baar, Switzerland for water containing KI) that are placed outside the CT pump the fluids through the HCC via FEP tubing that is connected to the inlets and outlet of the helical setups inside the CT. For each scan, a set of 2D X-ray projection images is acquired. Each set consists of projection images acquired at different rotation angles ω, which are obtained by rotating the sample stage by $\Delta\omega$ = 0.25° after the acquisition of each X-ray projection. The spatial resolution is 18 µm.

2.2 Image Processing

The image processing workflow is depicted schematically in Fig. 3. For each scan, the resulting set of X-ray projection images (1) is reconstructed to a set of voxel slices along the z direction (2), using the commercially available reconstruction software NRecon (Bruker, Billerica, MA). In the reconstruction step, also scanning artifacts are reduced. Reorganization of the data is necessary (2a) to obtain cross-sectional views of the capillary (2b) along the angle of revolution of the helix ϕ. A binary mask is applied to the cross-sectional images, such that only voxels inside the tube are retained (3). The 16-bit gray values of the remaining voxels are converted into mass fractions (4) using linear calibration functions. As scanning artifacts deteriorate the uniformity of gray values in the whole measurement domain, calibration curves are captured ϕ-wise. More details on the determination of calibration curves are given in the Supporting Information.

3 Results and Discussion

3.1 Data Evaluation

3.1.1 Artifacts

Scanning artifacts are disturbances in the reconstructed images that result from imaging and reconstruction. Fig. 4 gives reconstructed x-y and x-z slices at exemplary reference positions y_{ref} and z_{ref} in the HCC (p_1) that are filled with a homogeneous liquid ($w_{KI} = 0$, $w_{KI} = 0.2$). As can be seen from the figure, regions that are expected to be represented by a homogeneous gray value are disturbed by artifacts (A). The primary artifacts visible here are ring artifacts (A1), beam hardening (A2), and streak artifacts (A3).

Ring artifacts originating from ill-calibrated or defect detector elements (A1) [26] appear as concentric circles around the center of the rotation axis. The disturbance is most significant in the center of rotation, hence the center of the reconstructed image. The measurement section of the HCC is distant (d_c/2) from the center of rotation. Here, the effects of ring artifacts do not affect the concentration profile significantly.

Beam hardening arises from a filtering effect on the polychromatic X-ray beam induced by the sample [26]. It is visible by a decreasing gray value profile towards the center of the image. Fig. 4 shows that beam hardening can be eliminated sufficiently for low KI mass fractions, as can be seen from the plateaus in the gray value profiles. However, for higher KI mass fractions, beam hardening is still visible for a KI mass fraction of $w_{KI} = 0.2$. The beam hardening correction that proofed to be sufficient for pure water is insufficient for correction of beam hardening of other (denser) materials. However, all reconstructions have to be performed with the same beam hardening correction value to avoid systematic calibration errors.

The whole reconstructed volume is affected by streak artifacts (A3) that arise from a combination of scattering and beam hardening [26]. They are caused by the experimental setup itself, meaning the FEP tube, the support structure, and the liquid inside the tube. The more complex the setup (lower pitch means more turns in the helix) and the higher the KI mass fraction, the stronger the streak effect.

3.1.2 Low Contrast Detectability

The low-contrast detectability specifies the limit at which a low-contrast object with a specific size can be distinguished from its background. The low-contrast limit can be calculated using a statistical method [31]. A quadratic object with a specified edge length (l_p) can be differentiated from its background with a confidence level of 95 % if the low-contrast limit $> 3.29\,\sigma_{bg}$, given that the mean gray values of object and background follow a Gaussian distribution with standard deviation σ_{bg}. The low-contrast limit is determined slice-wise along the main flow direction and averaged across all slices. In the present experiments, the σ_{bg} increases with the mass fraction of KI and therefore is not identical for the background and the sample object.

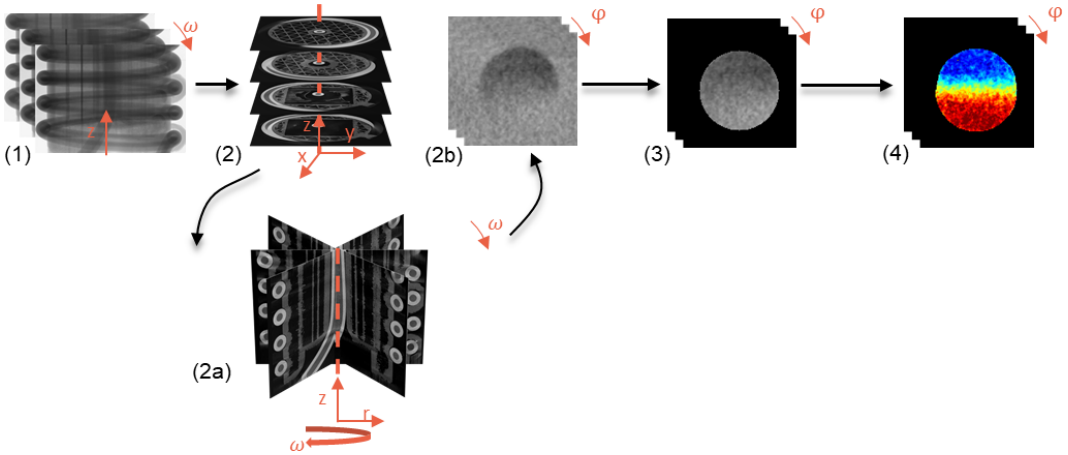

Figure 3. Schematic of the image processing routine. (1) Sets of X-ray projection images. (2) Reconstructed set of voxel slices. (2a) Reorganization of data to voxel slices normal to the main flow direction (2b). (3) Segmentation of voxel slices to obtain the region of interest. (4) Mass fractions of KI in water.

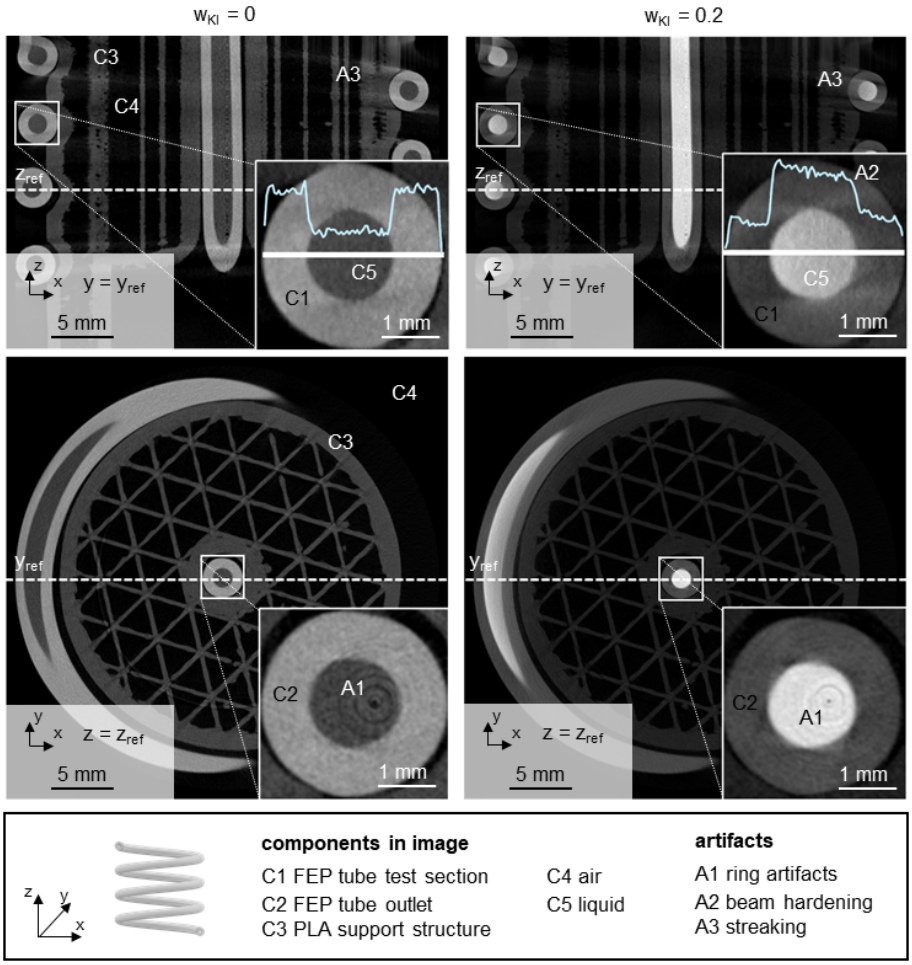

Figure 4. Visualization of artifacts for exemplary *x-y* and *x-z* cross-sectional slices after beam hardening correction (p = 4.8 mm). The light blue profiles give the qualitative evolution of 16-bit gray values along the white solid lines in the rectangular ROIs.

The low-contrast limit given in Fig. 5 is a worst-case estimate of calculated with the highest expectable mass fraction. The low-contrast limit generally decreases with increasing object size. To track a small fluid portion with an edge length of 0.054 mm (3×3 voxels) for a maximum KI mass fraction of w_{KI} = 0.03 the 95 % confidence level is given for $\Delta w_{KI} \approx 0.01$. In this case, at least two mass fraction levels can be distinguished with high certainty, which would be too low for tracking Dean vortices. For w_{KI} = 0.06, the 95 % confidence level is between $\Delta w_{KI} \approx 0.013$ (p_1) and $\Delta w_{KI} \approx 0.01$ (p_2), meaning that at least four to five mass fraction levels can be distinguished. For w_{KI} = 0.2, the minimum mass fraction difference is Δw_{KI} = 0.05 for p_1 and Δw_{KI} = 0.03 for p_2, which also results in at least four mass fraction levels being clearly distinguishable.

An interesting conclusion for the study of flows in helices is that increasing the mass fraction of the tracer to a certain degree is necessary to obtain at least three distinguishable mass fraction levels. However, artifacts become more dominant with increasing KI mass fraction, and the distinguishability of high- and low-concentration regions in the cross sections does not improve further. For the current investigations follows that the initial concentrations chosen (w_{KI} = 0.05, w_{KI} = 0.15) are sufficient to allow the distinction of more than three to four mass concentration levels with a confidence of at least 95 %.

3.2 Phenomenological Observations

Starting from ϕ = 0°, Fig. 6 exemplarily demonstrates how iodide is transported across the capillary cross section of the HCC with p_1. All cross sections show iodide-poor and iodide-rich regions that are differently pronounced, differently arranged, and more or less sharply segregated. Relative deviations between adjusted and measured average mass fractions in the presented slices are below 2.5 % for $w_{KI,0}$ = 0.05 and below 0.4 % for $w_{KI,0}$ = 0.15. For the low initial tracer concentration ($w_{KI,0}$ = 0.05) and the lowest flow velocity ($\dot{V}$ = 1.5 mL min^{-1}, Re = 23, Dn = 5, T^* = 436), a sharp separation area exists between the iodide-poor and iodide-rich region, which is inclined to the inner wall (IW) at the beginning of the first coil (ϕ = 0°).

The cross-sectional concentration field is still affected by the secondary flow imposed by the first contact of the liquids in the

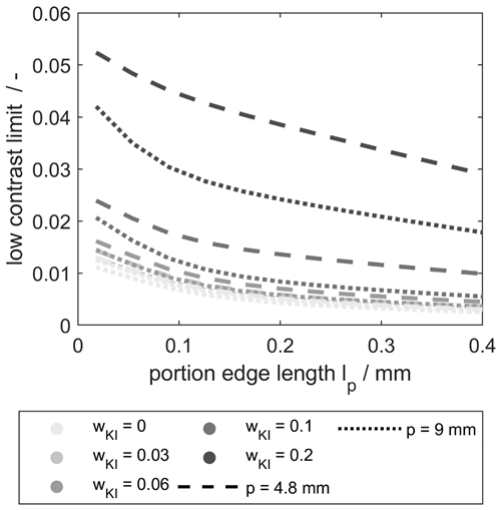

Figure 5. Low contrast detectability (LCD) depending on the highest expectable mass fraction.

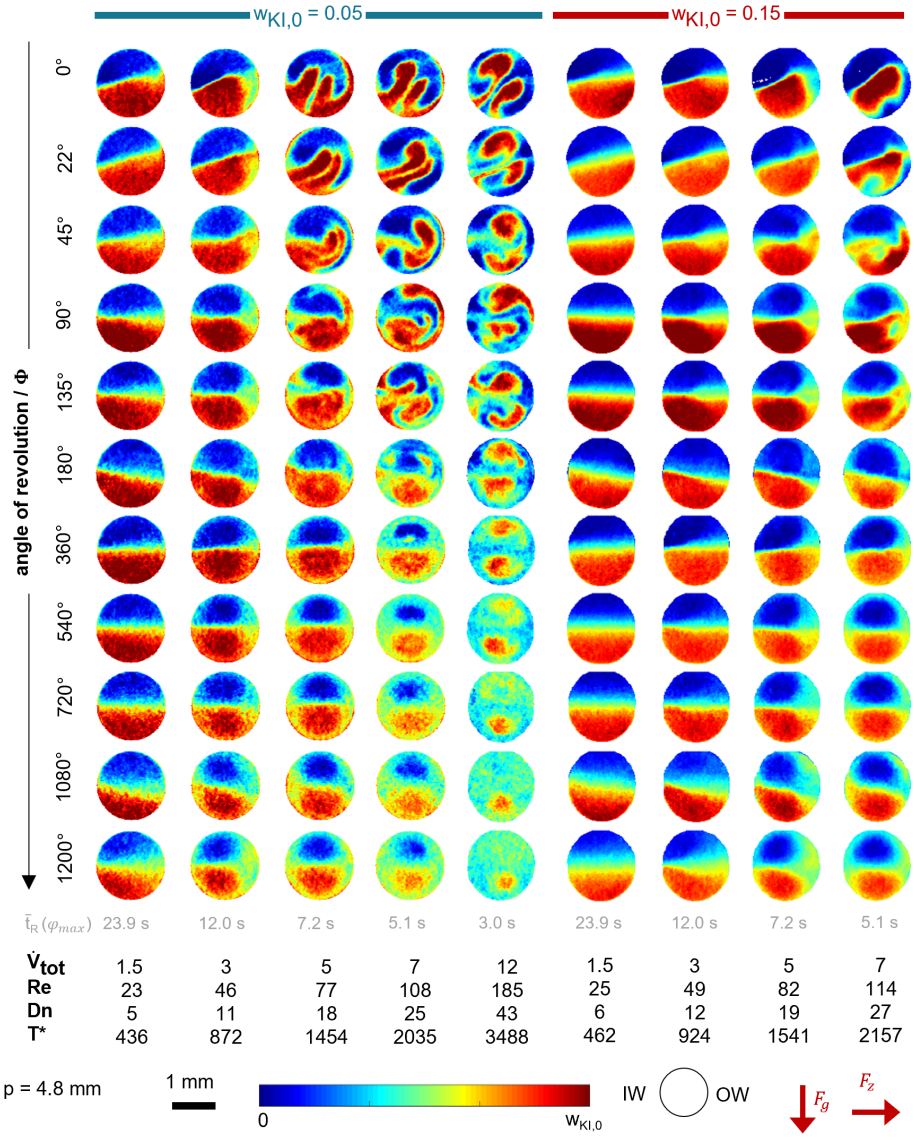

Figure 6. Exemplary visualization of cross-sectional concentration profiles at different angles of revolution ϕ for p_1 = 4.8 mm. F_g is the gravitational force, F_z is the centrifugal force.

T-junction and the transition section between the T-junction and first coil (see Fig. 2). Within the first coil, the separation area becomes horizontal and uniformly sharp due to a settling effect that arises from different densities of iodide-poor and iodide-rich liquid. In the second and third coil, secondary flow leads to the disturbance of the concentration field at ϕ = 360°. The cross section at ϕ = 1200° shows a distinction between iodide-poor liquid in the upper half and the iodide-rich liquid in the lower part of the cross section. However, the transition between the regions is relatively gradual, especially near OW. The shapes of the iodide-rich and the iodide-poor region allow conclusions about the nature of the secondary flow in the cross sections.

The concentration fields indicate two vortices of approximately the same size that rotate in opposite directions, the lower of which rotates in the clockwise direction. However, the concentration profile does not correspond to a fully established Dean flow. While the secondary flow at low *Re* is sufficient to entrain some iodide-rich liquid into the upper half of the tube at OW, it is insufficient to transport it along the inner tube wall back to IW, such that iodide settles close to OW.

At a volume flow rate of $\dot{V}$ = 7 mL min^{-1} (*Re* = 108, *Dn* = 25, T* = 2035, $w_{KI,0}$ = 0.05), the concentration fields differ significantly from the field at low *Re*. Although at ϕ = 0° an iodide-rich and iodide-poor region can be easily distinguished, the iodide-rich liquid is no longer restricted to the bottom half of the capillary cross section. Instead, the regions have an irregular shape that originates from flow momentum induced before ϕ = 0°. At ϕ = 360°, the concentration field is relatively uniform and resembles a concentration profile that is characteristic for Dean flow, as already published by several authors [10, 21, 32].

The iodide-rich region at the bottom and the iodide-poor region at the top are surrounded by a significant amount of liquid with intermediate iodide concentration. In the second and third coil, the characteristic of the concentration field remains, but radial mixing progresses as intermediate regions grow, and iodide-poor and iodide-rich regions shrink. For the highest volume flow rate tested ($\dot{V}$ = 12 mL min^{-1}, *Re* = 185, *Dn* = 43, T* = 3488, $w_{KI,0}$ = 0.05), the Dean flow intensifies further which leads to nearly complete mixing at ϕ = 1200°.

Similar phenomenological observations can be made for $w_{KI,0}$ = 0.05 and $w_{KI,0}$ = 0.15. As the density difference between pure water and solution is higher at $w_{KI,0}$ = 0.15 ($\Delta\rho_{rel} \approx 12\,\%$) as for $w_{KI,0}$ = 0.05 ($\Delta\rho \approx 4\,\%$), the gravitational force is more pronounced and inhibits mixing. The effect of secondary forces is lower in the transition section for lower initial KI fractions, which is visible from a sharper segregation area. Furthermore, the transition to fully developed symmetric Dean flow is shifted to higher Dean numbers.

3.3 Mixing Quality

The mixing quality α is calculated for each ϕ using definition Eq. (4) [33], where σ_{max} is the variance of a totally segregated distribution, see Eq. (5). The maximum mass fraction w_{max} of the X-ray tracer is set to $w_{max} = w_{KI,0}$, the mean mass fraction $\bar{w}$ and standard deviation σ^2 are calculated in each cross section.

$$\alpha = 1 - \sqrt{\frac{\sigma^2}{\sigma^2_{max}}} \tag{4}$$

$$\sigma^2_{\dot{V},max} = (0.5 w_{max})^2 \tag{5}$$

Fig. 7 shows exemplary mixing qualities for a helix with p_1 for the different initial tracer concentrations. The evolution of mixing quality corresponding to mass fraction profiles in Fig. 6 is given in Fig. 7. Generally, the curves for higher *Re* progress on a higher level than curves for lower *Re*, which is caused by the mixing in the inlet section. Even though the progression of α is perturbated by local artifacts, an overall increase with increasing ϕ is visible. Due to the relatively short capillary lengths within the measurement sections, the mixing quality at the maximum observable ϕ is still low for most *Re*. Only at *Re* = 108 and *Re* = 185 at $w_{Ki,0}$ = 0.05 higher mixing qualities are reached at ϕ = 1200° as the Dean flow significantly accelerates mixing. Comparing $w_{KI,0}$ = 0.05 and $w_{KI,0}$ = 0.15 reveals that the increase in α is stronger for lower $w_{KI,0}$.

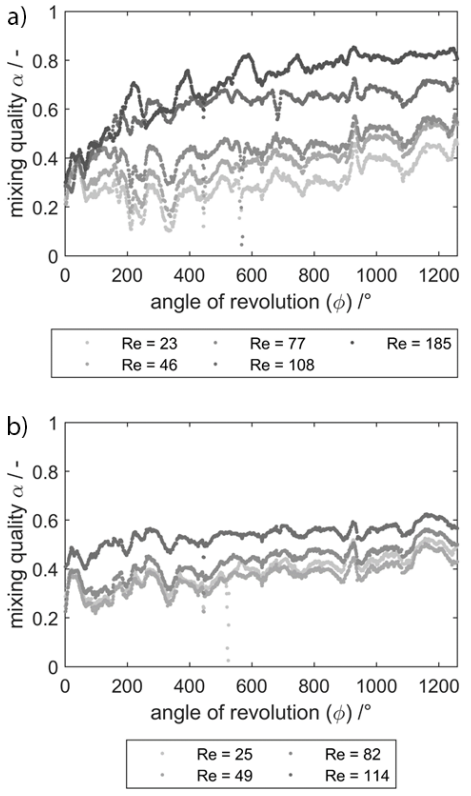

Figure 7. Mixing quality in cross-section over angle of revolution ϕ for p_1 = 4.8 mm. (a) $w_{KI,0}$ = 0.05, (b) $w_{KI,0}$ = 0.15.

The exemplary evolution of α over ϕ does not account for the different residence times resulting from the different volume flow rates. To compare radial mixing efficiency for different flow conditions while accounting for the different residence times, an equivalent radial dispersion coefficient D_{eq} is defined. D_{eq} can be interpreted as the theoretical diffusion coefficient necessary to cause the same increase in α in a diffusion experiment as that in α caused by secondary flow in a helix. Further information about the calculation of D_{eq} is given in the Supporting Information.

As displayed in Fig. 8, D_{eq} rises with increasing *Re* and is higher for lower $w_{KI,0}$. For *Re* < 60, no significant effect of *p* on D_{eq} can be found. At higher *Re*, D_{eq} becomes increasingly higher for p_2 than for p_1, which is contrary to findings from the literature where a higher pitch is reported to have a reducing effect on mixing efficiency. It should be noted that the standard deviation for the highest *Re* is high, and conclusions about a possible additional gravity effect should be drawn with caution.

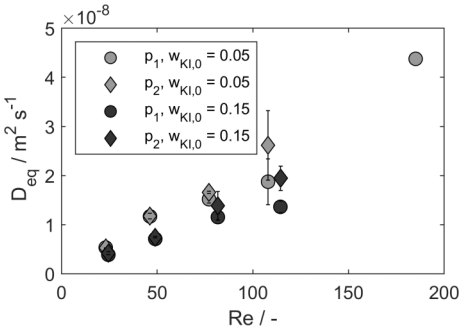

Figure 8. Equivalent radial dispersion coefficient D_{eq} (with standard deviation) as a function of *Re*.

4 Conclusion

Tomographic measurements are conducted for flow experiments in helically coiled tubes (23 < *Re* < 185, 5 < *Dn* < 43) for different initial tracer concentrations ($w_{KI,0}$ = 0.05, $w_{KI,0}$ = 0.15). The methodology yields cross-sectional mass fraction fields along the main flow direction. Dean vortices can be observed that intensify with increasing *Re* and decreasing contribution of gravity. The analysis of the mixing quality and the derivation of an equivalent mixing coefficient support the qualitative observations.

The main challenge in analyzing concentration fields and drawing quantitative conclusions is the high noise level caused by scanning artifacts. Contributing factors are the complexity of the setup and the initial mass fraction of the tracer. The amount of tracer must be high enough to allow at least three different mass fraction levels. However, too high a concentration does not necessarily lead to better distinguishability due to the increasing presence of artifacts. Furthermore, a higher tracer concentration leads to a change in fluid properties.

While the density difference between pure and tracer-enriched liquid might enable the investigation of gravity-related effects, an undistorted investigation is barely possible. Altogether, micro-computed tomography was found to offer

great potential for investigating steady laminar mixing in capillaries. Future research will concentrate on a more detailed investigation of the interplay of curvature, gravity, and torsion in a helically coiled capillary, and the present investigations will be enriched by numerical simulations.

Supporting Information

Supporting Information for this article can be found under DOI: https://doi.org/10.1002/ceat.202100530.

Acknowledgment

The authors acknowledge the German Research Foundation (DFG, grant number INST 212/397-1) that granted the Bruker Skyscan 1275. Furthermore, we acknowledge financial support by German Research Foundation (DFG) and TU Dortmund University within the funding program Open Access Publishing. Additionally, thanks are given to RJL Micro & Analytic, Karlsdorf-Neuthard, Germany, for technical support and training. Finally, we would like to acknowledge C. Schrömges (Laboratory of Equipment Design, TU Dortmund University, Germany) for technical advice. Open access funding enabled and organized by Projekt DEAL.

The authors have declared no conflict of interest.

Symbols used

d_c	[m]	coil diameter
d_i	[m]	inner diameter
Dn	[–]	Dean number
d_o	[m]	outer diameter
f	[–]	flow direction
F_g	[kg m s^{-2}]	gravitational force
F_z	[kg m s^{-2}]	centrifugal force
D_{eq}	[m^{2}s^{-1}]	equivalent dispersion coefficient
I	[W m^{-2}]	intensity of X-rays
I_0	[W m^{-2}]	initial intensity of X-rays
l_p	[m]	portion edge length
p	[m]	pitch
Re	[–]	Reynolds number
s	[m]	thickness of sample
T	[°C]	temperature
T^*	[–]	modified torsion parameter
u	[m s^{-1}]	flow velocity
$\dot{V}$	[m^{3}s^{-1}]	volume flow rate
w	[–]	mass fraction of KI
x	[m]	spatial coordinate
y	[m]	spatial coordinate
Z	[–]	atomic number
z	[m]	spatial coordinate

Greek letters

α	[–]	mixing quality
μ	[m^{-1}]	linear attenuation coefficient
ν	[m^{2}s^{-1}]	kinematic viscosity
ρ	[kg m^{-3}]	density
σ	[–]	standard deviation
φ	[°]	angle of revolution
ω	[°]	angle of rotation

Abbreviations

FEP	fluorinated ethylene propylene
HCC	helically coiled capillary
IW	inner wall
LCD	low contrast detectability
OW	outer wall
ROI	region of interest

Subscripts

bg	background
max	maximum

References

[1] N. Kockmann, *Transport Phenomena in Micro Process Engineering*, Springer, Berlin **2008**.
[2] *Coulson and Richardson's Chemical Engineering*, 7th ed., Vol. 18: *Heat and Mass Transfer: Fundamentals and Applications* (Eds: R. P. Chhabra, V. Shankar), Butterworth-Heinemann **2018**.
[3] S. Vashisth, V. Kumar, K. D. P. Nigam, *Ind. Eng. Chem. Res.* **2008**, *47 (10)*, 3291–3337. DOI: https://doi.org/10.1021/ie701760h
[4] W. R. Dean, *London Edinburgh Dublin Philos. Mag..J. Sci.* **1927**, *4 (20)*, 208–223. DOI: https://doi.org/10.1080/14786440708564324
[5] C. Y. Wang, *J. Fluid Mech.* **1981**, *108*, 185–194. DOI: https://doi.org/10.1017/S0022112081002073
[6] M. Germano, *J. Fluid Mech.* **1982**, *125 (1)*, 1. DOI: https://doi.org/10.1017/S0022112082003206
[7] H. C. Kao, *J. Fluid Mech.* **1987**, *184*, 335–356. DOI: https://doi.org/10.1017/S002211208700291X
[8] S. Klutz, S. K. Kurt, M. Lobedann, N. Kockmann, *Chem. Eng. Res. Des.* **2015**, *95*, 22–33. DOI: https://doi.org/10.1016/j.cherd.2015.01.003
[9] S. Kim, S. J. Lee, *Exp. Fluids* **2009**, *46 (2)*, 255–264. DOI: https://doi.org/10.1007/s00348–008–0555–8
[10] S. Litster, J. G. Pharoah, N. Djilali, *Heat Mass Transfer* **2006**, *42 (5)*, 387–397. DOI: https://doi.org/10.1007/s00231–005–0029–y
[11] L. Sharma, K. Nigam, S. Roy, *Chem. Eng. Sci.* **2017**, *160*, 227–235. DOI: https://doi.org/10.1016/j.ces.2016.11.034
[12] S. P. Vanka, G. Luo, C. M. Winkler, *AIChE J.* **2004**, *50 (10)*, 2359–2368. DOI: https://doi.org/10.1002/aic.10196
[13] A. K. Saxena, K. D. P. Nigam, *Chem. Eng. Commun.* **1983**, *23 (4–6)*, 277–289. DOI: https://doi.org/10.1080/00986448308940479
[14] M. Brito, P. Sanches, R. M. L. Ferreira, D. I. C. Covas, *J. Hydraul. Eng.* **2017**, *143 (3)*, 4016087. DOI: https://doi.org/10.1061/(ASCE)HY.1943–7900.0001253

[15] A. Jain, D. Ewing, C. Y. Ching, *Exp. Therm Fluid Sci.* **2019**, *107*, 88–106. DOI: https://doi.org/10.1016/j.expthermflusci.2019.05.007
[16] Y. Li, X. Wang, B. Zhou, S. Yuan, S. K. Tan, *Int. J. Heat Fluid Flow* **2017**, *68*, 189–202. DOI: https://doi.org/10.1016/j.ijheatfluidflow.2017.10.011
[17] P. Kováts, F. J. W. A. Martins, M. Mansour, D. Thévenin, K. Zähringer, *Exp. Fluids* **2020**, *61*, 117. DOI: https://doi.org/10.1007/s00348–020–02950–6
[18] A. Kalpakli Vester, S. S. Sattarzadeh, R. Örlü, *J. Visualization* **2016**, *19 (2)*, 261–273. DOI: https://doi.org/10.1007/s12650–015–0310–1
[19] D. L. Mejia Mendez, C. Lemaitre, C. Castel, M. Ferrari, H. Simonaire, E. Favre, *J. Membr. Sci.* **2017**, *530*, 20–32. DOI: https://doi.org/10.1016/j.memsci.2017.02.016
[20] K. V. Bulusu, M. W. Plesniak, *Int. J. Heat Fluid Flow* **2018**, *73*, 143–153. DOI: https://doi.org/10.1016/j.ijheatfluidflow.2018.08.002
[21] P. Kováts, C. Velten, M. Mansour, D. Thévenin, K. Zähringer, *Exp. Fluids* **2020**, *61*, 203. DOI: https://doi.org/10.1007/s00348–020–03035–0
[22] J. Schuler, L. M. Neuendorf, K. Petersen, N. Kockmann, *AIChE J.* **2021**, *67 (2)*, e17111. DOI: https://doi.org/10.1002/aic.17111
[23] K. Keshmiri, M. Pourmohammadbagher, H. Huang, N. Nazemifard, *Fuel* **2019**, *235*, 1327–1336. DOI: https://doi.org/10.1016/j.fuel.2018.08.108
[24] Y. Nakashima, *Eng. Geol.* **2000**, *56 (1–2)*, 11–17. DOI: https://doi.org/10.1016/S0013–7952(99)00130–1
[25] J. Schuler, J. Herath, N. Kockmann, *J. Flow Chem.* **2021**, *21*, 217–222. DOI: https://doi.org/10.1007/s41981–021–00161–6
[26] T. M. Buzug, *Computed Tomography: From Photon Statistics to Modern Cone-Beam CT with 10 Tables*, Springer, Berlin **2008**.
[27] F. C. Kracek, *J. Phys. Chem.* **1931**, *35 (4)*, 947–949. DOI: https://doi.org/10.1021/j150322a002
[28] A. Cioncolini, L. Santini, *Exp. Therm Fluid Sci.* **2006**, *30 (4)*, 367–380. DOI: https://doi.org/10.1016/j.expthermflusci.2005.08.005
[29] P. Novotny, O. Sohnel, *J. Chem. Eng. Data* **1988**, *33 (1)*, 49–55. DOI: https://doi.org/10.1021/je00051a018
[30] D. E. Goldsack, R. Franchetto, *Can. J. Chem.* **1977**, *55 (6)*, 1062–1072. DOI: https://doi.org/10.1139/v77–148
[31] J. Hsieh, *Computed Tomography: Principles, Design, Artifacts, and Recent Advances*, 2nd ed., Vol. 188, Wiley Interscience, SPIE Press, Hoboken, NJ **2009**.
[32] M. Mansour, P. Khot, D. Thévenin, K. D. Nigam, K. Zähringer, *Chem. Eng. Sci.* **2020**, *214*, 114522. DOI: https://doi.org/10.1016/j.ces.2018.09.046
[33] S. Dreher, M. Engler, N. Kockmann, P. Woias, in *Micro and Macro Mixing* (Eds: D. Mewes, F. Mayinger, H. Bockhorn, W. Peukert, H.-J. Warnecke), Heat and Mass Transfer, Springer, Berlin **2010**.

